Journal of Zhejiang University-SCIENCE A 2025 26(12):1179-1196
www.jzus.zju.edu.cn; www.springer.com/journal/11582
E-mail: jzus_a@zju.edu.cn

Research Article
https://doi.org/10.1631/jzus.A2500209

Elliptical ultrasonic side milling for improved surface integrity and fatigue resistance of thin-walled Ti6Al4V components

Lianxing LIU[1,2], Xinggang JIANG[1,2], Enze YING[1,2], Zhefei SUN[1,2], Daxi GENG[1,2]✉, Deyuan ZHANG[1,2]✉

[1]*School of Mechanical Engineering and Automation, Beihang University, Beijing 100191, China*
[2]*Institute of Bionic and Micro-Nano Systems, Beihang University, Beijing 100191, China*

Abstract: Ti6Al4V alloy is critical for thin-walled aerospace components, yet conventional methods for its surface enhancement struggle to balance efficiency and precision. While ultrasonic vibration milling has been demonstrated to improve fatigue performance, its strengthening mechanism requires further investigation. Additionally, its application in fatigue-critical side milling remains underexplored. To address this gap, we introduce the method of ultrasonic peening side milling (UPSM), which integrates elliptical vibration into side milling to achieve simultaneous machining and surface strengthening. Theoretical and finite element analyses are performed to elucidate the mechanisms of residual stress generation and plastic deformation in UPSM and two-pass UPSM (TUPSM). Our experimental results demonstrate that the UPSM method reduces surface defects. At a vibration amplitude of 8 μm, UPSM increases the surface residual compressive stress by 47.4% and the thickness of subsurface plastic deformation layer by 91.5% as compared to conventional milling (CM). TUPSM amplifies these effects, achieving a 55.5% increase in residual compressive stress. Fatigue tests reveal 3.38-fold (for UPSM) and 3.76-fold (for TUPSM) improvement in fatigue life over CM, a phenomenon which is attributed to the subsurface crack initiation and grain refinement induced by ultrasonic ironing and impact effects. This work establishes UPSM as an integrated and cost-effective solution for enhancing fatigue performance in thin-walled Ti6Al4V components, overcoming the limitations of conventional methods and advancing between precision machining and strengthening treatments.

Key words: Ultrasonic peening side milling (UPSM); Ti6Al4V; Surface integrity; Fatigue performance; Thin-walled components

1 Introduction

As the most widely used type of titanium alloy, Ti6Al4V is often utilized in the manufacturing of large load-bearing components for aircraft wings, fuselages (Shamoto and Moriwaki, 1999; Liao et al., 2021), and engines (Medvedev et al., 2021; Zhang et al., 2022). This is due to its large specific strength, excellent corrosion resistance, and high resistance to fatigue and impacts. However, Ti6Al4V parts frequently encounter severe high-frequency vibrations and cyclic loads in operational conditions (Lu et al., 2022; Wang et al., 2022). Therefore, developing cost-effective and robust methods for strengthening Ti6Al4V components is crucial for ensuring the overall lifespan and reliability of aircraft (Xue et al., 2023). Common metal surface enhancement techniques include shot peening, laser shock peening, and ultrasonic rolling. While shot peening and laser shock peening both can achieve significant strengthening effects, they tend to induce surface roughening, and they create challenges in process control (Lu et al., 2021; Qin et al., 2023). As revealed in varying studies, surface roughening induced by the uneven distribution of pits from shot peening (Qin et al., 2023; Yao et al., 2024) or laser shock peening (Sun et al., 2024) typically results in surface roughness exceeding 0.8 μm. Conversely, Liu et al. (2025) demonstrated that rotary ultrasonic elliptical milling maintains surface roughness below 0.8 μm across varying amplitudes, i.e., within the typical range of precision machining. Ball burnishing and ultrasonic rolling have also been shown to improve surface quality. Rodríguez et al. (2012, 2019, 2020) validated ball burnishing on aluminum alloys,

✉ Deyuan ZHANG, zhangdy@buaa.edu.cn
Daxi GENG, gengdx@buaa.edu.cn
Lianxing LIU, https://orcid.org/0009-0003-2848-4465
Daxi GENG, https://orcid.org/0000-0003-3591-4630

Received May 25, 2025; Revision accepted July 6, 2025;
Crosschecked Nov. 5, 2025; Online first Dec. 11, 2025

demonstrating concurrent surface roughness reduction and residual stress enhancement with high efficiency. However, the application of such techniques to thin-walled side-milled structures remains undocumented. Moreover, these strengthening methods require additional processing steps and incur higher costs, hindering their application to large titanium alloy components in aircraft, and particularly to thin-walled structures (Wang et al., 2019; Wang Y et al., 2024). Furthermore, de la Maza García et al. (2025) developed a tensile prestress-assisted machining technique that simultaneously improves surface roughness, dimensional accuracy, and post-unloading residual compressive stress, offering new avenues for thin-wall strengthening. However, challenges in implementation tend to persist for geometrically complex thin-walled components.

In the past few decades, ultrasonic vibration cutting (UVC) has garnered widespread attention and seen significant application in precision machining. This is because it allows for intermittent cutting (Moriwaki and Shamoto, 1995; Shamoto and Moriwaki, 1999), which offers advantages such as reduced cutting force (Wang GY et al., 2024; Ying et al., 2024), enhanced process stability (Sun et al., 2024), improved tool durability (Liu et al., 2019), higher surface quality (Pang et al., 2021), and improved surface roughness (Celaya et al., 2010). Recently, researchers have found that UVC can also achieve considerable surface hardening during finishing operations. When the vibration tool includes a component perpendicular to the machined surface, the ultrasonic ironing and impact effects of the cutting edge can produce better strengthening than methods with a single direction of vibration, such as longitudinal vibration milling (Brehl and Dow, 2008; Yang et al., 2020; Li et al., 2023; Lü et al., 2023). Li et al. (2020) investigated the ultrasonic turning of Ti6Al4V, and found that the impact of the cutting edge in the direction normal to the workpiece surface effectively improves the surface hardness, residual compressive stress, and thickness of the plastic deformation layer. Specifically, a 10.4-fold increase in fatigue life was achieved at a vibration amplitude of 8 μm, with the fatigue sources shifting to the subsurface. Suárez et al. (2016, 2019) examined the fatigue strengthening effects of ultrasonic-assisted face milling on Ni-alloy 718 through four-point bending fatigue tests, and achieved fatigue life improvements of 12.00% to 14.74% under a vibration amplitude of 1.5 μm. Moreover, Teimouri and Grabowski (2024) selected a larger vibration amplitude range for longitudinal vibration end milling on Inconel 718, and discovered that a vibration amplitude of 8 μm resulted in a 3-fold increase in fatigue life compared to conventional milling (CM). However, recent research on the impact of normal ultrasonic cutting on fatigue performance enhancement has mainly focused on ultrasonic turning and the use of longitudinal vibration for end milling surface enhancement. In contrast, side milling enhancement, which is a more widely used machining method for critical fatigue areas in thin-walled titanium alloy structures, has received less attention.

In summary, although some scholars have achieved fatigue resistance enhancement using UVC in end milling and turning, fatigue resistance enhancement using ultrasonic vibration cutting for side milling remains poorly understood, despite it being more commonly encountered in the critical fatigue areas of thin-walled components. Therefore, researching the fatigue resistance enhancement effects of ultrasonic peening side milling (UPSM) and revealing its enhancement mechanisms holds significant theoretical and practical value. Accordingly, in this study, we propose a novel surface strengthening method involving side milling, and examine the surface enhancement effects and fatigue performance of Ti6Al4V under different vibration amplitudes and reinforcement cycles with UPSM.

First, a 2D cutting simulation was employed to investigate the cutting and strengthening mechanisms under different milling processes, with the distribution characteristics of residual compressive stress being compared. Then, experiments were conducted with different chip morphologies. The geometric features of the machined surface were analyzed from the perspectives of 2D surface morphology, 3D surface morphology, and surface roughness. We also undertook a comparative study of the surface enhancement effects of UPSM from the perspectives of the thickness of plastic deformation layer and the surface residual compressive stress. Our experimental findings validate the effectiveness of UPSM in improving the fatigue performance of Ti6Al4V alloy, while also demonstrating its potential as a novel surface enhancement technique for aerospace-grade titanium components with high demands for fatigue resistance.

2 Theoretical analysis of UPSM

2.1 Kinematic analysis of UPSM

As shown in Fig. 1, two equal-amplitude vibrations perpendicular to the mill's axis are applied to the end mill. The two vibrations are perpendicular to each other, and have a phase difference of 90°, resulting in an elliptical vibration trajectory that rotates in the same direction as the rotation of the mill cutter. Taking the initial position of the center of the end mill as the origin O, we establish a planar XOY coordinate system. The feeding motion occurs in the X-direction. In this diagram, a_e is the uncut chip thickness, and a_p is the milling depth. The movement trajectory of the UPSM tool tip can be calculated as Eq. (1):

$$\begin{cases} x_0 = r\sin\left(\dfrac{2\pi n}{60}t - i\delta\right) + A\sin\left(2\pi ft + \dfrac{2\pi n}{60}t\right) + \dfrac{nv_f Z}{60}t, \\ y_0 = r\cos\left(\dfrac{2\pi n}{60}t - i\delta\right) + A\cos\left(2\pi ft + \dfrac{2\pi n}{60}t\right), \end{cases} \tag{1}$$

where x_0 and y_0 are the motion coordinates of the cutting edge; r is the radius of the end mill; t is the cutting time; $\delta = 2\pi/Z$, where δ is the angle between two adjacent tool tips, and Z is the total number of tool tips; i (i=1, 2, ⋯, Z) is the serial number of the selected tool tip; n is the rotating speed of the tool holder; v_f is the feeding speed of the workpiece; A is the vibration amplitude of the tool tip; f is the vibration frequency.

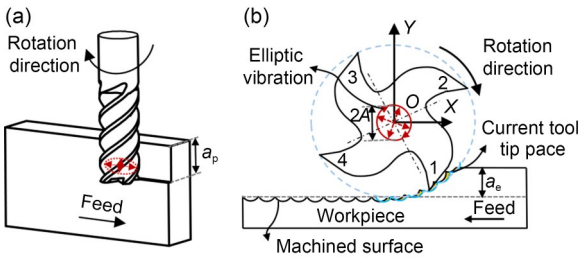

Fig. 1 Schematic diagram of UPSM: (a) 3D view; (b) 2D view

Due to the characteristics of the machined surface being determined by the cutting process of the cutting edge proximal to the final machined surface, the rotational motion of the cutting edge can be approximated as a translational motion along the X-direction when studying the impact of the tool tip's trajectory on the machined surface. Furthermore, the feeding speed v_f of the workpiece is negligible in comparison to the linear speed of the spindle rotation, as well as the speed of ultrasonic vibration. Thus, in the region near the final machined surface, the elliptical trajectory of the UPSM tool tip can be simplified to:

$$\begin{cases} x_0 = -\dfrac{2\pi nr}{60}t + A\sin(2\pi ft), \\ y_0 = A\cos(2\pi ft). \end{cases} \tag{2}$$

Following Eq. (2), the motion trajectories of the cutting edges in UPSM under different amplitudes are calculated and shown in Fig. 2. The elliptical vibration can be decomposed into components that are perpendicular and parallel to the machined surface. The perpendicular component causes overlapping trajectories of adjacent cutting edges, thereby achieving intermittent cutting, which significantly improves the cooling/lubrication efficacy and the cutting quality.

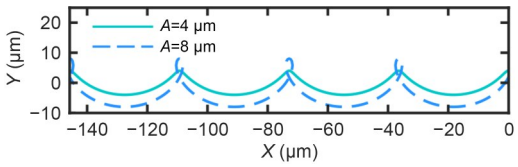

Fig. 2 Simplified movement trajectory for UPSM cutting edge

According to the simplified motion trajectory, the cutting and strengthening mechanisms in UPSM and two-pass UPSM (TUPSM) are shown in Fig. 3. TUPSM refers to a second-pass UPSM process performed on the initially UPSM-treated surface using micron-scale cutting widths. Liu et al. (2023) demonstrated in a study on ultrasonic peening drilling that the flank face exerts an ironing effect on the machined surface. The strengthening mechanism of UPSM primarily originates from flank face ironing and cutting-edge impact effects. TUPSM uniquely superimposes a second cycle of these effects—flank face ironing and cutting-edge impacting—onto the UPSM-processed surface, thereby achieving better strengthening.

2.2 2D finite element cutting simulation of UPSM

Due to challenges in experimentally observing the UPSM process, ABAQUS software was employed to investigate the cutting and strengthening mechanisms of both UPSM and TUPSM. A 2D cutting model is developed, which provides a straightforward and intuitive representation of the process. As shown in Fig. 4, a 2D

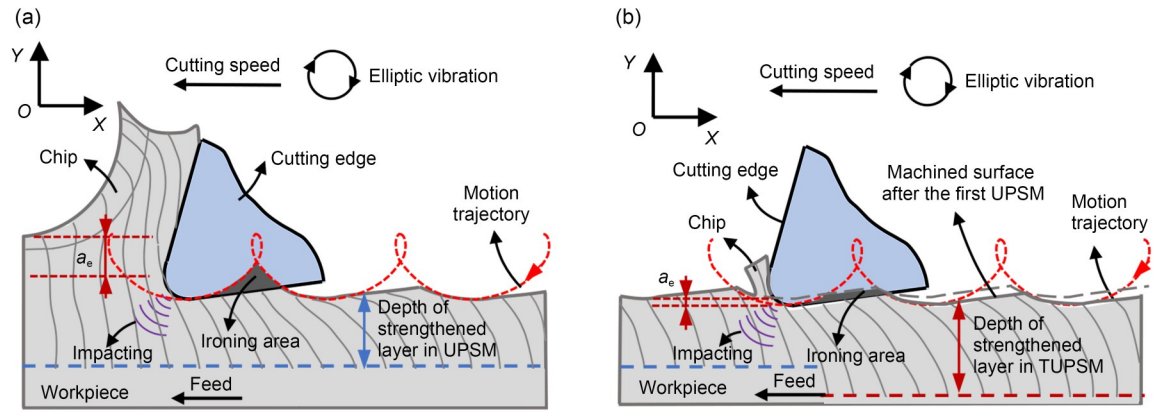

Fig. 3 Schematic diagram of surface topography and deformation in (a) UPSM and (b) TUPSM

model with dimensions of 160 μm×100 μm was established using Abaqus/Explicit 2021. The entire workpiece was discretized with CPE4R elements and divided into three regions: a 25 μm cutting layer with a uniform mesh size of 0.5 μm, a 20 μm subsurface layer with a graded mesh size ranging from 0.5–1.0 μm, and a 55 μm fixed base layer with a transitional mesh size of 1.0–8.0 μm, which are subjected to a fixed boundary constraint. Given the extremely short duration of the cutting process, tool wear was neglected in the simulation. The cutting tool was modeled as a rigid body with a reference point assigned to apply kinematic constraints and motion loads. The cutting edge has a 7° rake angle and a 10° relief angle, with an edge radius of 3 μm. The cutting speed of the tool is 40 m/min, the feed rate is 0.08 mm/r, and the ultrasonic vibration frequency is 18500 Hz. Two analysis steps were implemented to simulate the process in the TUPSM process. Complete details of the material constitutive model are provided in Section S1 of the electronic supplementary materials (ESM).

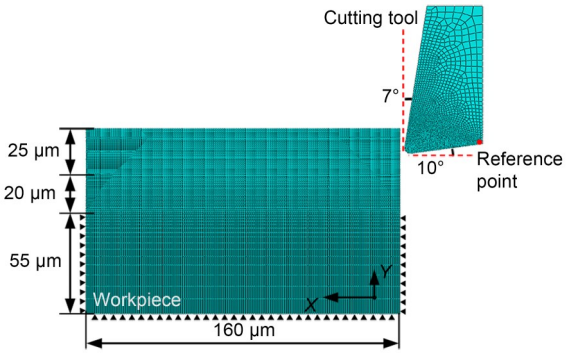

Fig. 4 2D finite element cutting simulation model

2.3 Strengthening mechanism in UPSM

2D finite element analysis (FEA) simulations can directly capture the stress evolution during the cutting process, enabling quantitative analysis of strengthening mechanisms. As shown in Fig. 5a, the high-stress zones in conventional cutting are primarily concentrated near the cutting edge (excluding the primary deformation zone). As the tool advances, the stress near the cutting edge increases abruptly, leading to shear failure. Material above the separation line forms chips, while the remaining material is ironed by the edge radius and flank face to generate the machined surface.

In the ultrasonic peening cutting process, the cutting edge's motion is initiated from the highest point, and the process can be divided into three stages: penetration, downward pressing, and upward withdrawal, which are illustrated in Fig. 5b. During penetration, the cutting edge is driven obliquely downward into the workpiece, with an average cutting speed that is higher than conventional cutting. This causes the high-stress zone on the workpiece surface to be significantly deepened from the edge's impact. As penetration continues, the tool's flank face comes into direct contact with the workpiece, resulting in instantaneous negative-relief-angle cutting. At this stage, both the edge's extrusion effect and the flank face's ironing effect occur simultaneously, maximizing the extent of the high-stress zone. The depth of influence from edge extrusion and flank face ironing increases with both the angle between the cutting edge's instantaneous velocity and the workpiece's horizontal plane, as well as the cutting speed magnitude. When the cutting edge reaches the lowest point of its trajectory, the cutting speed direction becomes parallel to the workpiece's horizontal

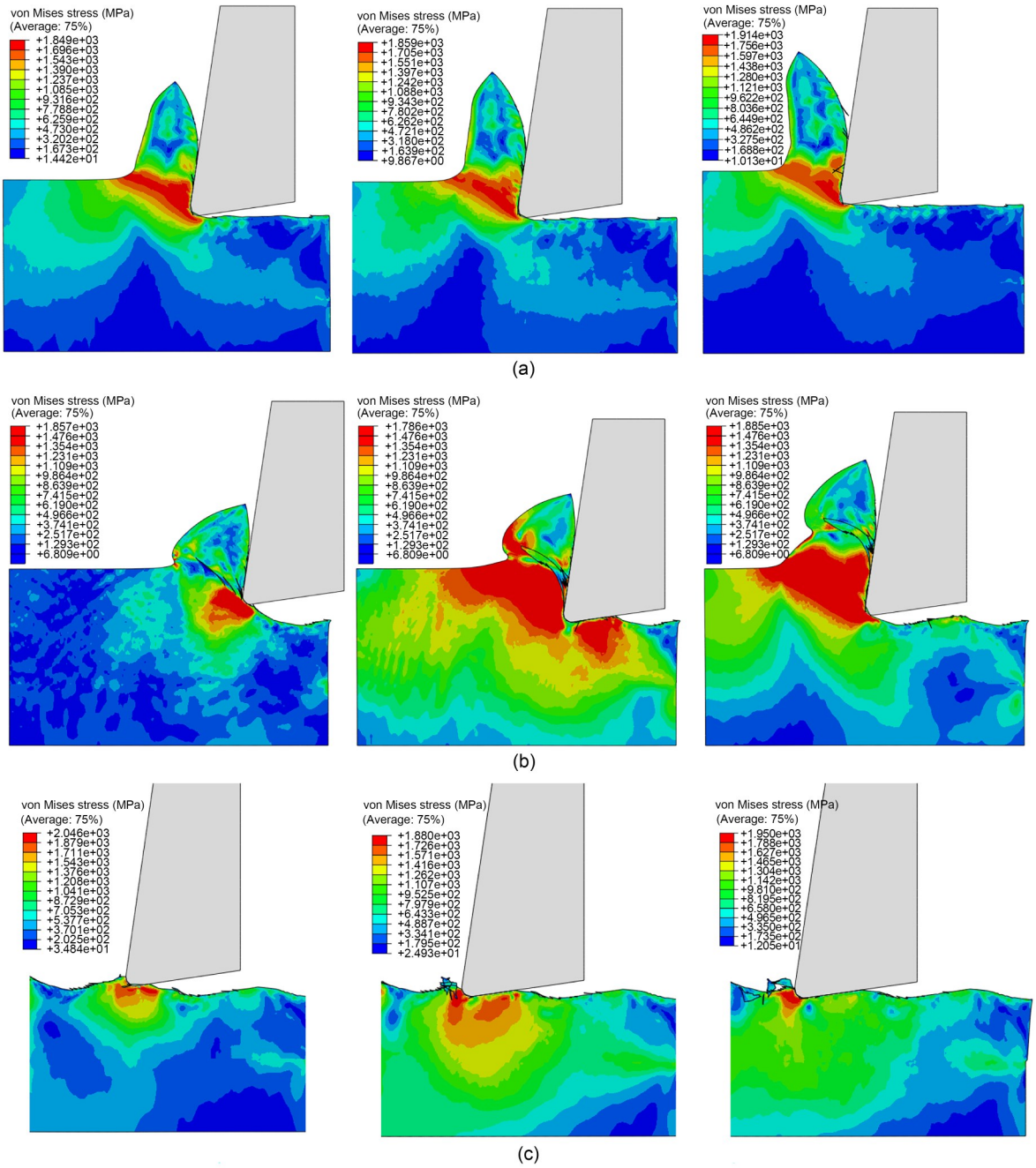

Fig. 5 Stress distribution nephograms under different cutting parameters: (a) conventional cutting; (b) ultrasonic peening cutting with A=8 μm; (c) two-pass ultrasonic peening cutting with A=8 μm. References to color refer to the online version of this figure

direction, exhibiting the same strengthening mechanism as conventional cutting. However, since the cutting speed peaks at this moment, the depth of the high-stress zone remains greater than in conventional cutting. Subsequently, as the cutting edge moves upward, the ironing effect from the flank face disappears, and the extrusion effect from the edge radius diminishes. Meanwhile, a tensile stress zone is generated near the trough of the vibration-induced cutting marks; this is due to the upward pull of the edge. However, the magnitude of this tensile stress is far lower than the compressive stress produced during the impact and ironing of the cutting edge.

During the two-pass ultrasonic peening cutting process, as shown in Fig. 5c, the cutting edge exerts a

shearing and ironing effect on the already machined surface as it removes a small amount of material. This leads to further strengthening of the machined surface.

Analyses of plastic deformation evolution (PEEQ) and residual stress distributions (S11, the residual stress value in the feed direction) under ultrasonic peening cutting, including comparisons of single-pass/two-pass processing and amplitude effects, are provided in Section S2 of the ESM. This discussion validates the superposition mechanism of two-pass strengthening and characterizes depth-resolved residual stress profiles under different processing conditions.

3 Experimental procedure

3.1 Materials

The workpiece material used in this study is Ti6Al4V. To facilitate observation of the subsurface grain deformation, a basket-weave Ti6Al4V was selected, as shown in Fig. 6, and the mechanical properties of this Ti6Al4V are presented in Table 1.

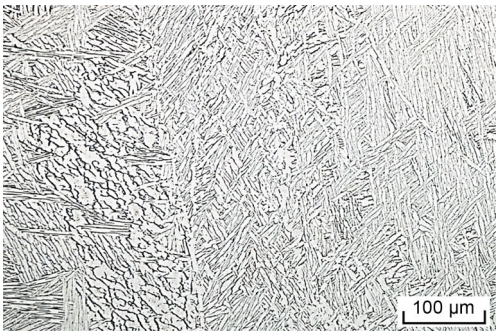

Fig. 6 Representative microscopic image of the Ti6Al4V microstructure

Table 1 Thermo-mechanical properties of the Ti6Al4V alloy

Parameter	Value
Density (kg/m^3)	4429
Hardness (HV)	285
Elastic modulus, E (GPa)	114
Poisson's ratio, v	0.33
Yield strength (MPa)	860
Tensile strength (MPa)	960

3.2 Test system and parameters

The tests were conducted using a custom-made ultrasonic elliptical milling BT50 tool holder, installed on a triaxial vertical machining center (BV100). Side milling was performed with a climb milling approach, as illustrated in Fig. 7. A water-based cutting fluid was employed. The ultrasonic elliptical cutting system is comprised of two key components: a biphasic ultrasonic signal generator and a dual-bend elliptical ultrasonic transducer. The signal generator produces ultrasonic signals with a phase difference of 90°, allowing independent power adjustment of each signal. The ultrasonic transducer consists of two sets of piezoelectric ceramic elements, an amplitude rod, a front cover, and a rear cover, with the milling tool integrated into the amplitude rod. Ultimately, two bending vibrations in the directions of radial depth of cutting and feeding, with identical frequencies and a 90° phase difference, are generated on the milling tool. These vibrations combine to create an elliptical vibration that is perpendicular to the axial direction of the milling tool, with a frequency of 18500 Hz. This elliptical vibration ensures that the milling cutter generates normally-oriented impacts on the side-milled surface at any angular position during rotation. When the ultrasonic signal generator is turned off, the system operates as CM. The parameters in the surface integrity test are detailed in Table 2. In the experiments, the TUPSM involved performing a second pass of milling on the machined surface of the initial milling, maintaining a cutting width of 3 μm. Given the small 3 μm cutting width in TUPSM, the machine spindle was positioned directly on the reference surface from the previous UPSM process for the tool setting errors. Under these conditions, the machine tool precision, tool runout, and alignment errors are effectively minimized. Each group was tested at least three times to ensure experimental accuracy. The milling cutter used in this experiment is a four-flute solid carbide end mill, with specific parameters shown in Table 3.

In the surface integrity tests, the workpiece was cut into dimensions of 30 mm×26 mm×5 mm. To ensure the reliability of the measurements, three to five points were selected along the feeding direction. A super-depth-of-field microscope (VHX7000, KEYENCE, Japan) was used to capture the 2D morphology. The surface roughness was measured using a probe-type meter (SJ-410, Mitutoyo, Japan). A white light interference microscope (NexView8300, Zygo, Japan) was employed to obtain the 3D morphology and to acquire 3D point data. Residual stress on the surface was

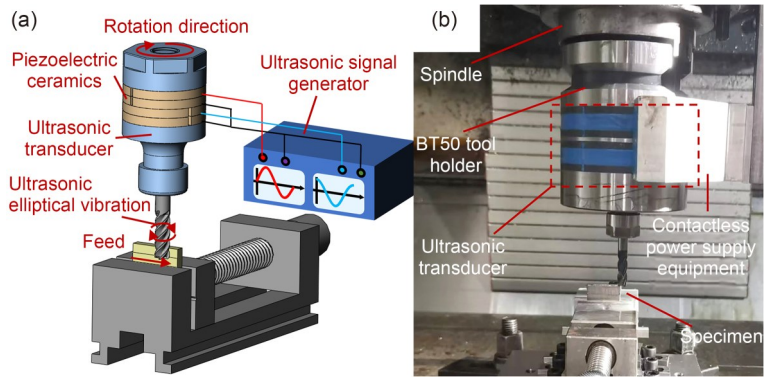

Fig. 7 Experimental setup of the surface integrity text: (a) schematic; (b) actual platform

Table 2 Cutting parameters of CM, UPSM, and TUPSM

Cutting parameter	CM	UPSM	TUPSM
Milling speed, v_c (m/min)	40	40	40
Feed rate per tooth, f_z (mm/z)	0.02	0.02	0.02
Radial depth of cut, a_e (mm)	0.100	0.100	0.003
Axial depth of cut, a_p (mm)	5	5	5
Vibration amplitude, A (μm)	0	4, 8	8
Vibration frequency, f (Hz)	18500	18500	18500

Table 3 Specification of the end mill

Tool parameter	Description
Coating	TiAlN
Spiral length (mm)	25
Cutting edge	4
Diameter (mm)	10
Helix angle (°)	37
Rake angle of side edge (°)	7
Relief angle of side edge (°)	10

assessed using X-ray diffractometry (AutoMATE II, Rigaku, Germany) for nondestructive testing, with a beam diameter of 3 mm. Finally, samples with a length of 6 mm were obtained along the feeding direction using wire cutting. After metallographic preparation and polishing, the samples were etched with an etching solution composed of HF:HNO_3:H_2O in a ratio of 1:2:47. The subsurface deformation was then observed using a scanning electron microscope (Sigma500, ZEISS, Germany).

The fatigue life test was conducted using an electromagnetic high-frequency fatigue testing machine (QBG 150, Qianbang, China). The dimensions of the specimen and the fatigue test setup are shown in Fig. 8. Fatigue specimen blanks were produced via milling, retaining a 0.1 mm machining allowance across all

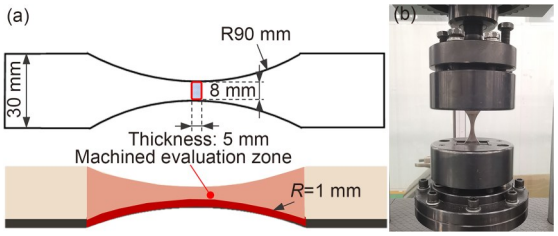

Fig. 8 (a) Specimen geometry of fatigue test and test scheme; (b) tensile fatigue test setup

surfaces for subsequent finishing operations. The final critical section is a rectangular cross-section of 8 mm× 5 mm. As shown in Fig. 8a, all surfaces except the clamping regions underwent precision side milling. Custom fixtures ensured positioning accuracy and system rigidity, while chatter was effectively prevented during finishing because of the adequate structural stiffness and optimized cutting parameters. The cutting parameters and tools are the same as those used in the surface integrity test, and are detailed in Tables 2 and 3. To prevent premature fatigue failure at the edges, which could affect the accuracy of the results, the edges were rounded using a tool with an inner radius (R) of 1 mm. During the fatigue test, the stress ratio was set to 0.1, with a frequency of approximately 85 Hz and a maximum stress (σ_{max}) of 770 MPa. Each set of parameters included three to five fatigue specimens, and the fatigue fracture surface was observed using an electron microscope.

4 Results and discussion

4.1 Chip morphology

The UPSM achieves surface strengthening during precision machining, where material removal and strengthening occur simultaneously. Chip morphological

analysis serves as an effective indicator for comparative investigation of material removal mechanisms under varying UPSM conditions. In Fig. 9, the chip morphology under different conditions is compared, and the chip formation process is qualitatively described through the 2D cutting simulations. Insights into how the cutting process occurs are revealed by the chip morphology. Chips produced in CM have a relatively flat macroscopic appearance, with small curvature, slight surface wrinkles, and good uniformity.

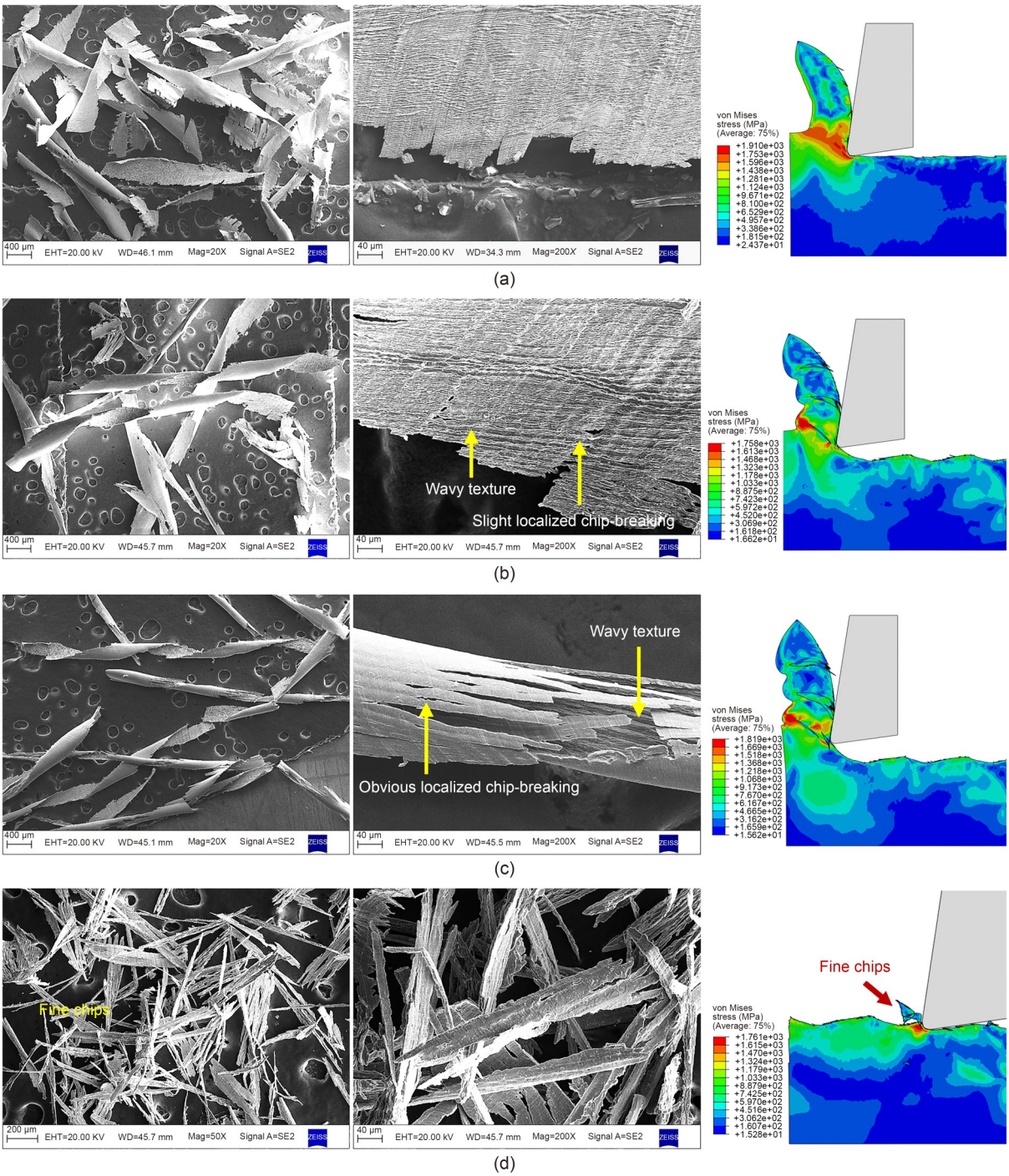

Fig. 9 Chip morphology under varying cutting conditions: (a) CM with a_e=100 μm; (b) UPSM with A=4 μm and a_e=100 μm; (c) UPSM with A=8 μm and a_e=100 μm; (d) TUPSM with A=8 μm and a_e=3 μm. References to color refer to the online version of this figure

The macro-scale morphology of the UPSM chips is characterized by curling features, while the micro-scale surface exhibits textures associated with vibratory cutting. It is presumed that the surface vibration textures alter the mechanical properties of the chips, resulting in their curling appearance at a macro-level. Additionally, at a vibration amplitude of 4 μm, slight localized chip-breaking features are observed in certain areas, while obvious localized chip-breaking features appear at a vibration amplitude of 8 μm.

TUPSM produces fragmented and fine chips, primarily due to the significantly larger vibration amplitude of the tool relative to the cutting thickness. This results in periodic separation during cutting. Moreover, the fine nature of the chips makes them prone to secondary fracturing along the *Z*-direction, ultimately leading to the formation of broken and small chips. This also indicates that UPSM enables variable-thickness machining, thereby potentially enhancing micro-cutting capabilities. Even when using a cutting thickness of 3 μm, the instantaneous cutting thickness exceeds the minimum cutting thickness, allowing the cutting edge to undergo shear cutting.

4.2 Surface topography and surface roughness

Fig. 10 illustrates the 2D and 3D surface topographies resulting from different milling methods, showing their macroscopic surface characteristics and cutting damage. It can be observed that the surfaces from all milling methods are relatively smooth, with no visible feed marks. This is attributed to the small feeding speed per tooth used, which renders the feed marks undetectable. From the 2D surface morphology, it is evident that the surface obtained through CM is relatively flat; however, it does exhibit defects such as scratches and scales. Additionally, slight discoloration is observed, which may be attributed to friction and thermal effects during cutting.

In contrast, the surfaces resulting from UPSM and TUPSM exhibit typical textural characteristics consisting of regular ridge marks. The slight and unavoidable discrepancies in the motion paths of the four cutting edges result in a primary spacing of the vibration traces that is equal to the distance traveled by the cutting edge during one vibration cycle. Notably, the UPSM surface contains secondary vibration traces between the primary traces, which are generated by the cutting actions of the other teeth of the milling cutter. In contrast, the TUPSM surface does not display distinct secondary vibration traces, which can be attributed to the uncut chip thickness during TUPSM is small; this prevents the formation of noticeable cutting marks. Additionally, UPSM significantly reduces surface defects such as scratches and scales, and there is no discoloration caused by the cutting heat. This improvement is attributed to the intermittent cutting effect produced by the elliptical vibration, which allows coolant to penetrate the cutting zone during each vibration cycle. This greatly enhances the cooling and lubrication effects, leading to improved surface cutting quality. From the

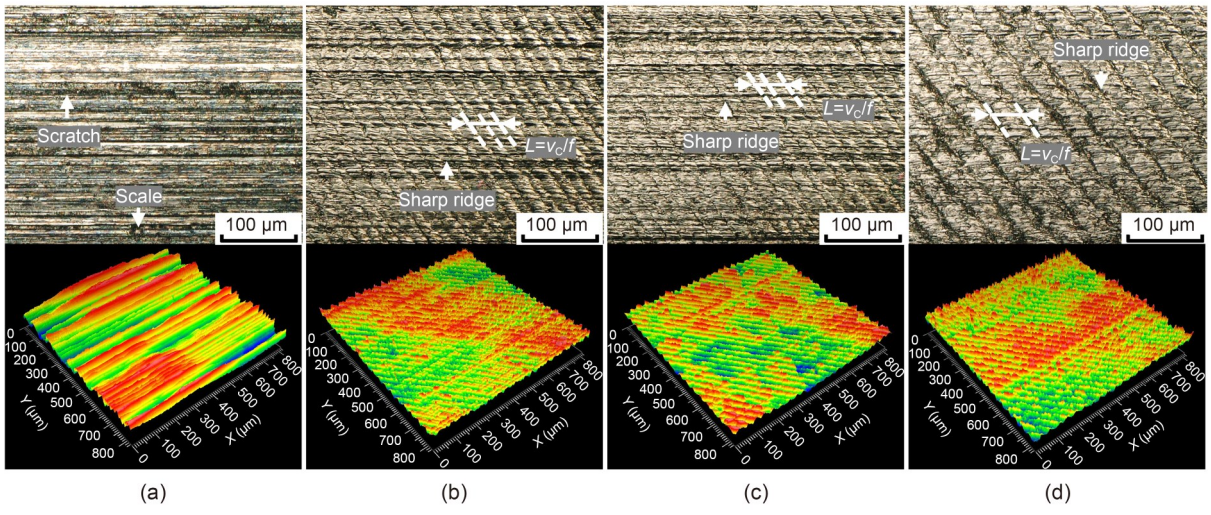

Fig. 10 2D and 3D surface topographies of the machined surface under different parameters: (a) CM; (b) UPSM with A= 4 μm; (c) UPSM with A=8 μm; (d) TUPSM with A=8 μm. L represents the distance that the cutting edge advances within one vibration cycle. References to color refer to the online version of this figure

3D surface morphology, it can be gleaned that both the UPSM and TUPSM surfaces exhibit regular vibration cutting marks compared to surfaces in CM, while also showing reduced overall surface fluctuation. This can be attributed to the high-frequency excitation of the vibrational cutting process, which alleviates the inherently unstable vibrations of the cutting system (Moriwaki and Shamoto, 1995; Zhang et al., 2021).

Fig. 11 presents a quantitative comparison of the surface morphology characteristics—in particular the surface roughness—under different milling methods, employing both the arithmetic average roughness (Ra) and the ten-point height (Rz) of the micro-irregularities. The Rz value is indicative of more extreme morphological features of the surface (Novovic et al., 2004). From Fig. 11, it is evident that both the Ra and Rz values for the UPSM surface are higher than those of CM, and they increase with larger vibration amplitude. This increase can be attributed to the residual height from the fluctuating cutting trajectory of UPSM. Although UPSM's slight roughness increase may elevate the stress concentration factor, this does not necessarily reduce the fatigue life, as the residual compressive stress distribution equally influences the outcome. Importantly, it has been observed in ultrasonic-assisted burnishing and ultrasonic vibration high-speed milling that, despite increased roughness, effective residual compressive stress improves fatigue life (Teimouri and Skoczypiec, 2024; Teimouri and Grabowski, 2025). It was further noted that fatigue life decreases when surface roughness rises significantly, without proportional strengthening benefits. This was evidenced in a multi-pass burnishing study where Pass 3 provided marginal residual stress improvement over Pass 2, but caused greater roughness deterioration, ultimately reducing the fatigue life (Teimouri and Grabowski, 2025). Notably, our surface roughness measurements for TUPSM show that Ra and Rz values are slightly higher than those of UPSM at the same vibration amplitude. This small elevation may be attributed to the extreme fineness of TUPSM-generated chips, which undergo greater plastic deformation during their formation, ultimately resulting in marginally higher residual ridges. It is important to note that although UPSM shows a slight increase in surface roughness compared to CM, the Ra value remains below 0.8, thus still categorizing this as a finishing process.

The results of our analyses of surface roughness and morphology indicate that, although the UPSM surface exhibits increased surface roughness due to the formation of a wavy surface texture, it concurrently has reduced defects, such as fewer surface scratches, scales, and thermal effects.

4.3 Surface residual stress

Fig. 12 compares the surface residual stress along the cutting speed direction for different milling methods. The cutting edge's force–thermal coupling effect on the machined surface can induce residual stress; when the cutting process effectively dissipates heat, it primarily manifests as residual compressive stress. As reported in Yuan et al. (2015) and la Monaca et al. (2021), residual compressive stress can mitigate part of the actual load when subjected to tensile fatigue loading, delaying surface crack initiation and propagation.

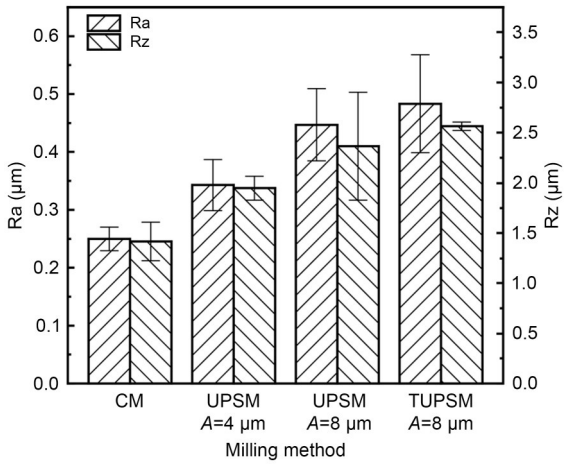

Fig. 11 Ra and Rz values under different milling methods

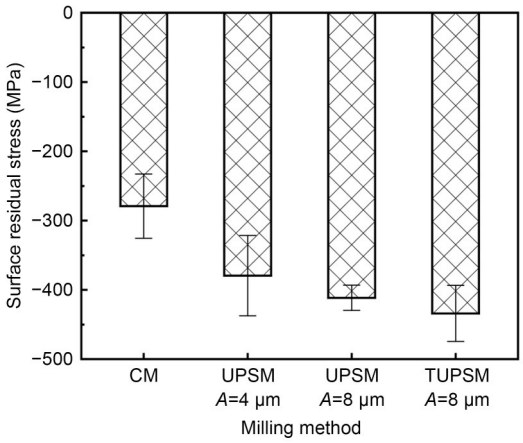

Fig. 12 Surface residual stress resulting from different milling methods

As shown in Fig. 12, all machined surfaces in the experiments exhibited residual compressive stress. This is attributed to the relatively small amount of cutting and the adequate cooling lubrication during the tests. UPSM significantly enhances the surface residual compressive stress as compared to CM, with this effect being more pronounced at a larger vibration amplitude. Specifically, at vibration amplitudes A=4 μm and A=8 μm, the residual compressive stress in UPSM increased by 36.0% and 47.4%, respectively, compared to CM. This enhancement is due to the ironing effect of the cutting edge and the ultrasonic impact effect in the direction of radial depth on the machined surface; larger vibration amplitudes lead to more ironing and impact effects, which is consistent with previous research (Zheng et al., 2018; Ni and Zhu, 2020). Moreover, Teimouri et al. (2019) observed that in ultrasonic surface burnishing studies, increased amplitude elevates the impact velocity, thereby deepening subsurface deformation zones. However, stress field redistribution after the impact does not necessarily produce significantly higher surface residual stress under certain conditions. Furthermore, TUPSM achieves even higher residual compressive stress than UPSM, displaying a 55.5% increase over CM. This indicates that second-pass processing in TUPSM applies additional ironing and impact effects directly onto the previously strengthened subsurface, thereby increasing surface residual compressive stress compared to UPSM.

4.4 Subsurface plastic deformation layer

Fig. 13 illustrates the subsurface plastic deformation layer under different milling methods. The force–thermal coupling effect during the cutting process leads to grain deformation and refinement. In the subsurface plastic deformation layer, dislocation accumulation also occurs, leading to grain refinement and enhanced surface strength. This phenomenon helps reduce the probability of surface crack initiation and slows the crack propagation rate. The depth of this layer is generally shallower than that of the residual compressive stress layer, and can serve as a direct indicator of surface strengthening effectiveness (Seenath and Sarhan, 2024). As indicated in Fig. 13, UPSM achieves a greater thickness of the subsurface plastic deformation layer compared to CM, with this enhancement increasing with the vibration amplitude. Specifically, at amplitudes A=4 μm and A=8 μm, the thickness increases by 51.5% and 91.5%, respectively. This improvement can be attributed to the ultrasonic ironing and impact effects present in UPSM. Additionally, TUPSM leads to a thicker plastic deformation layer compared to UPSM, with more pronounced subsurface grain deformation. This clearly demonstrates the cumulative strengthening effect of the second pass of TUPSM. Moreover, under UPSM, the subsurface grains are elongated and curved in the direction of the cutting speed, which aligns with the direction of tensile fatigue loading. Li et al. (2020) noted that grain refinement and fiberization of the machined surface can enhance the fatigue performance of components. The presence of a plastic deformation layer also increases the yield strength of the material's surface and reduces the likelihood of dislocation.

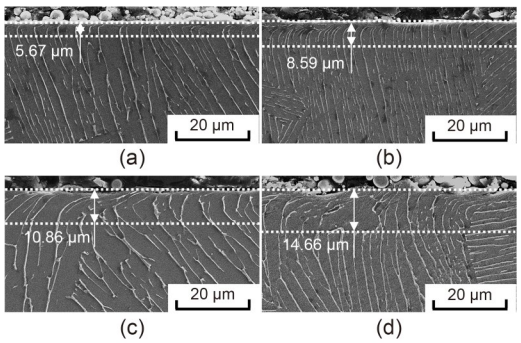

Fig. 13 Subsurface plastic deformation layer under different milling methods: (a) CM; (b) UPSM with A=4 μm; (c) UPSM with A=8 μm; (d) TUPSM with A=8 μm

4.5 Fatigue life and fracture analysis

Fig. 14 presents tensile fatigue lifetimes under different milling methods. The results indicate that UPSM

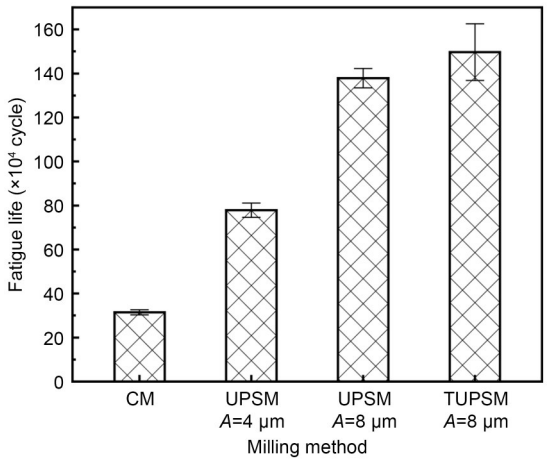

Fig. 14 Fatigue life under different milling methods

significantly increases the fatigue life of the specimens compared to CM. Additionally, within the experimental range, the fatigue improvement effect becomes more pronounced as the vibration amplitude increases. Specifically, at a vibration amplitude of A=4 μm, UPSM improves the fatigue life by a factor of 1.47 compared to CM, while at an amplitude of A=8 μm, the improvement factor is 3.38 times. Following TUPSM, the fatigue life improves further, showing a 3.76-fold increase compared to CM. This improvement arises from the cumulative strengthening effect of the sequential ultrasonic vibrations in the milling process. Based on integrated surface integrity and fatigue test results, we observe that although UPSM and TUPSM cause slight increases in surface roughness, they do enhance fatigue life. This phenomenon may be attributed to the stronger surface compressive stress layers and plastically deformed layers (oriented parallel to the loading direction), which are induced by increased vibration amplitudes and processing repetitions within our tested parameter range. These microstructural modifications alter the near-surface stress distributions, counteracting the negative effects of stress concentration and thereby delaying the initiation of cracking. Moreover, as vibration amplitude increases in UPSM, the normally-oriented impact and ironing forces exerted by the cutting edge intensify correspondingly, thereby elevating the surface strain rate of the workpiece (Liu et al., 2021). This amplifies both the surface residual compressive stress and the plastic deformation, thereby bolstering fatigue life enhancement effects.

Fig. 15 illustrates the fatigue fracture characteristics of specimens that underwent CM. From Figs. 15a and 15b, it can be observed that fatigue cracks originate from the surface, with more than three fatigue sources (green dashed lines) being present, one of which is a primary fatigue source. This is a key reason for the relatively low fatigue life of these specimens. The fatigue source cracks extend from different planes and converge, leading to a somewhat chaotic step-like texture on the fracture surface. In Fig. 15c, at approximately 500 μm from the fatigue source, the fracture surface exhibits noticeable unevenness, with many tearing ridges (orange dashed lines) being present. This complexity in the crack propagation directions is a result of multiple fatigue sources merging. Clear fatigue striations are visible, and the directions of these striations indicate the local crack propagation directions. Fig. 15c illustrates that at this cross-section, the crack propagation direction is quite complex. Additionally, numerous deeper secondary cracks (yellow dashed lines) can be observed. These secondary cracks are attributed to the complex local stress state, which results in stress levels in other directions exceeding those in the primary crack propagation directions. From Fig. 15d, it is evident that at about 1000 μm from the fatigue source, the fracture surface is relatively smooth, and the crack propagation direction is more consistent. There are noticeably fewer secondary cracks, and they are more shallow, which is because the enlargement of primary fatigue cracks allows for the convergence of the propagation directions of different fatigue sources. At this point, the system enters a stable crack propagation phase, which is characterized by increased stress along the primary crack propagation direction. Figs. 15c and 15d specify the total width and directions of five fatigue striations. It is noteworthy that at distances of approximately 500 and 1000 μm from the fatigue source, the total width of the fatigue striations does not show significant differences, both measuring around 0.4–0.5 μm. This indicates that the stress levels at these two positions are essentially the same during crack propagation.

Fig. 16 illustrates the fatigue fracturing characteristics of UPSM specimens at a vibration amplitude of A=4 μm. Figs. 16a and 16b reveal that there is only one fatigue source, which originates approximately 60 μm beneath the machined surface. The fatigue cracks display a radial pattern as they propagate outward, and the fracture surface appears relatively smooth. In Fig. 16c, at approximately 500 μm from the fatigue source, the fracture surface appears homogeneous. These fatigue striations indicate a relatively consistent crack propagation direction. Moreover, there are fewer and shallower secondary cracks observed in the cross-section, suggesting that the stress in the direction of the primary crack propagation is significantly higher at this location, and indicating that the system has entered a stable crack propagation phase. Fig. 16d shows that at about 1000 μm from the fatigue source, the crack propagation direction remains fairly uniform, and secondary cracks are minimal. At both 500 and 1000 μm, the total width of the fatigue striations are approximately 0.4 and 0.5 μm, respectively, indicating subtle differences in the crack propagation rates at these locations.

Fig. 17 illustrates the fatigue fracturing characteristics of UPSM specimens at a vibration amplitude of

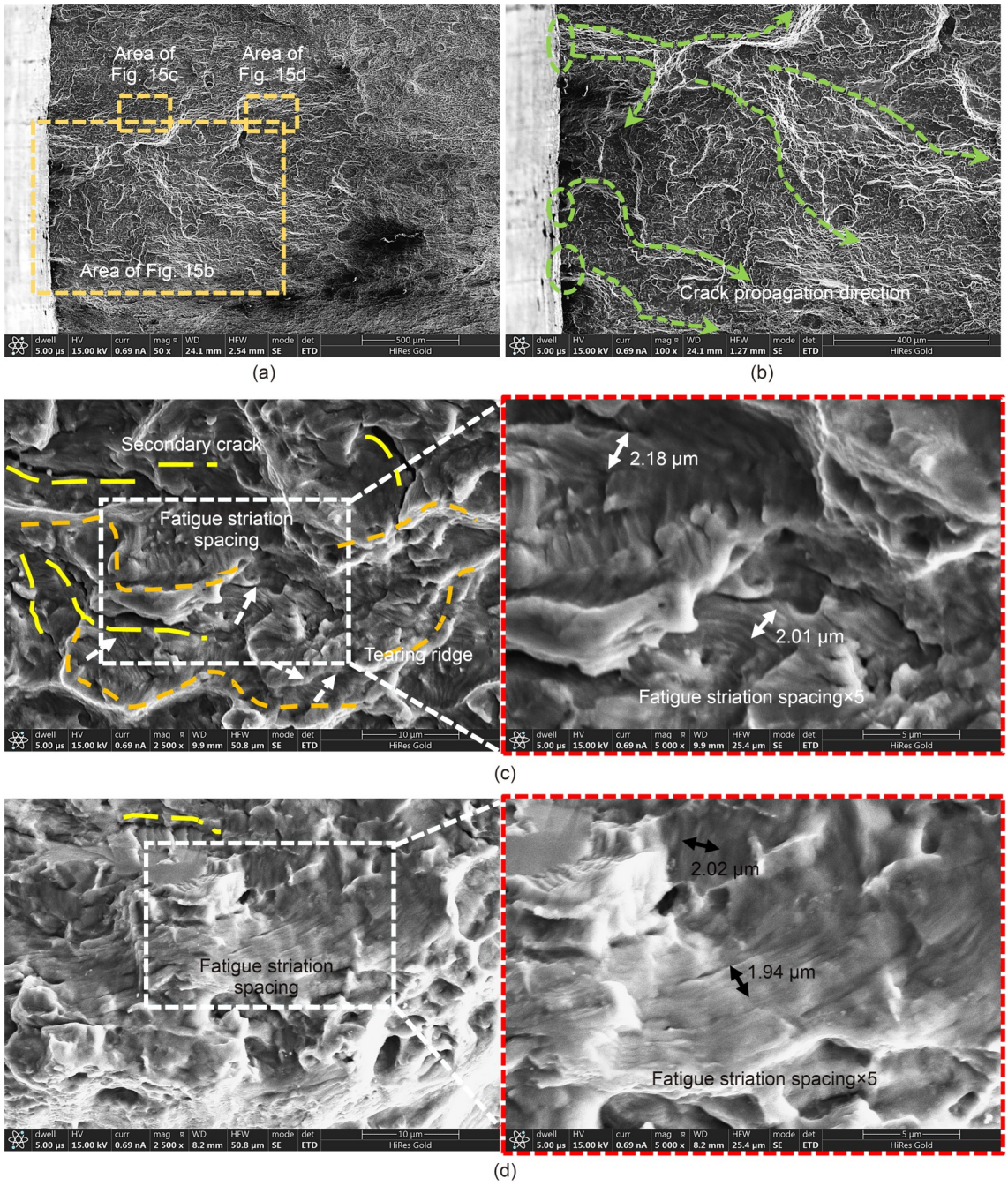

Fig. 15 Fatigue fracture characteristics of specimens under CM: (a) overall morphology of the fatigue source area; (b) distribution and growth paths of the fatigue source; (c) fatigue propagation approximately 500 μm from the fatigue source; (d) fatigue propagation approximately 1000 μm from the fatigue source. References to color refer to the online version of this figure

A=8 μm. From Figs. 17a and 17b, it is evident that the fatigue source originates from a region approximately 1000 μm beneath the machined surface, which is characterized by a singular eye-shaped fatigue source. The fatigue cracks radiate outward from this fatigue source, and the area surrounding the fatigue source exhibits a remarkably smooth surface. In Fig. 17c, at about 500 μm from the fatigue source, the fracture surface appears very flat, and distinct fatigue striations are difficult to identify. The total width of the fatigue striations at this position are approximately 0.3 μm, reflecting a very slow crack propagation rate. Additionally,

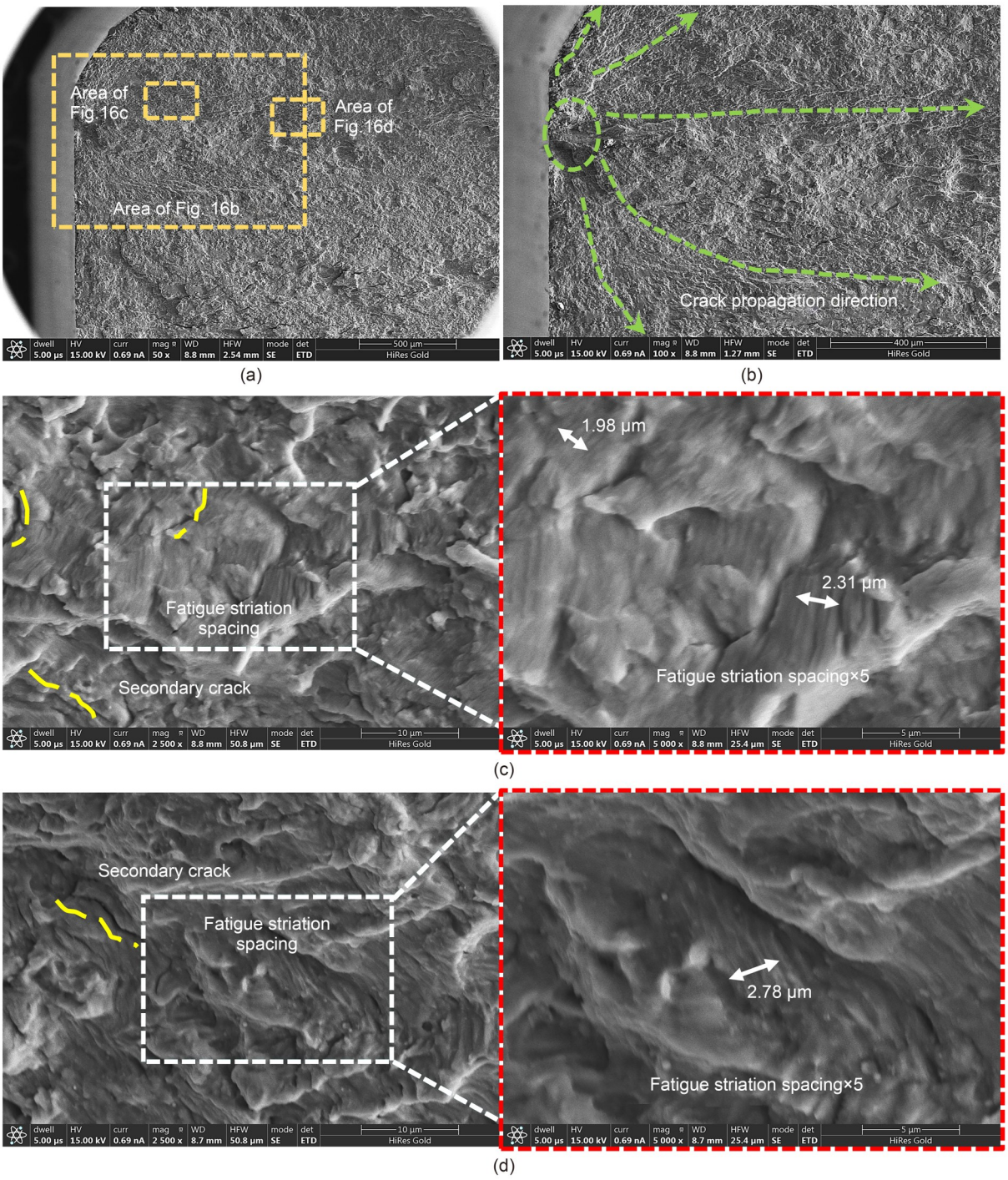

Fig. 16 Fatigue fracture characteristics of specimens under UPSM with A=4 μm: (a) overall morphology of the fatigue source area; (b) distribution and growth paths of the fatigue source; (c) fatigue propagation approximately 500 μm from the fatigue source; (d) fatigue propagation approximately 1000 μm from the fatigue source. References to color refer to the online version of this figure

there are numerous shallow secondary cracks at this fracture location. This phenomenon may be attributed to the internal origin of the fatigue source, which, during the initial stages of crack propagation, does not lead to significant plastic deformation. Consequently, the stress in the primary crack propagation direction is relatively similar to that in other directions, causing the formation of many secondary cracks. Fig. 17d shows the

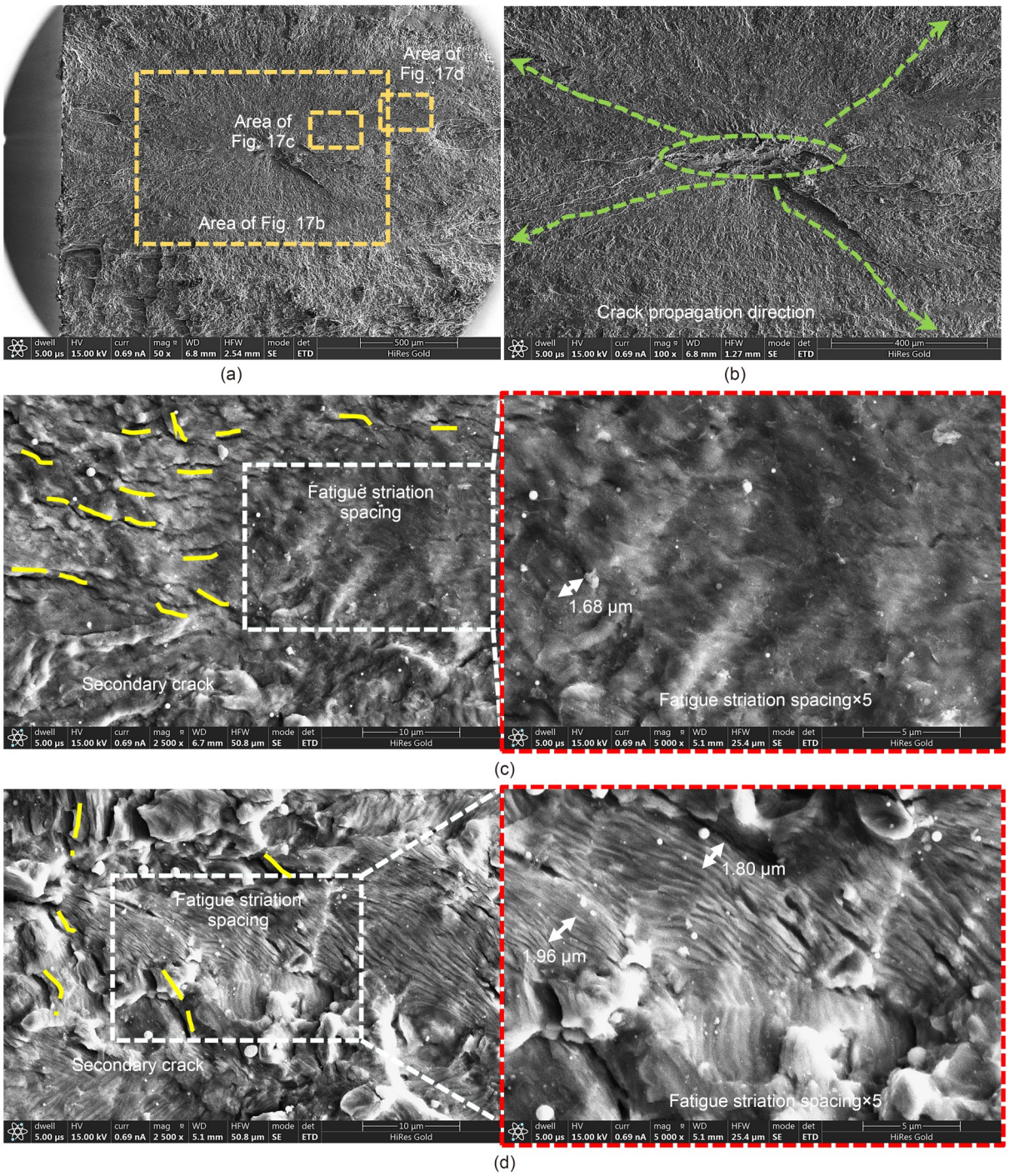

Fig. 17 Fatigue fracture characteristics of specimens under UPSM with A=8 μm: (a) overall morphology of the fatigue source area; (b) distribution and growth paths of the fatigue source; (c) fatigue propagation approximately 500 μm from the fatigue source; (d) fatigue propagation approximately 1000 μm from the fatigue source. References to color refer to the online version of this figure

fracture characteristics at approximately 1000 μm from the fatigue source. Here, a uniform pattern of fatigue striations is observed, with a notable decrease in the number of secondary cracks. The total width of the fatigue striations at this location are around 0.4 μm, indicating an increased crack propagation rate as the fracture enters a normal crack growth phase. This change is attributed to the larger size of the fatigue fracture at this

point, where significant stress concentration occurs in the direction of crack propagation during tensile loading. Overall, at a vibration amplitude of A=8 μm, the UPSM specimens exhibit favorable surface strengthening effects. The fatigue source arises from internal defects, resulting in a significantly slower initial crack propagation rate compared to cracks originating from the surface. The larger size of both the initiation and propagation areas contributes to a marked improvement in the fatigue life of the specimens.

Further fatigue fracture analyses of TUPSM specimens, which confirm internal crack initiation (~1700 μm below the surface) and demonstrate enhanced fatigue life through distinct propagation features (striation morphology and secondary crack), are detailed in Section S3 of the SEM. The fatigue source distribution and propagation behavior in TUPSM closely resemble those observed in UPSM with A=8 μm.

Figs. 15–17 and Fig. S3 of the SEM indicate that UPSM produces a significant overall strengthening effect on the surfaces of the specimens, causing the initiation sites of fatigue sources to shift from the surface to the subsurface. When the strengthening effect is more pronounced, fatigue sources can migrate to the interior of the material, thereby significantly enhancing both the fatigue life and the initial propagation life of the specimen. From a comparison of the total width of the fatigure striations, it can be inferred that UPSM does not cause a noticeable change in the total width of the fatigue striations. The total width of the fatigue striations ranges from 0.4 to 0.5 μm upon entering the normal crack propagation stage, indicating that the crack propagation rate of UPSM-treated specimen is comparable to that of CM-treated specimen in this stage. This phenomenon may arise because the surface-hardened layer generated by UPSM is relatively thin, which is insufficient to affect the stress distribution within the material. However, this characteristic does ensure that fatigue strengthening is achieved while avoiding significant dimensional inaccuracies for thin structures, due to the release of large compressive stress.

5 Conclusions

The effects of UPSM on the surface strengthening and fatigue performance of Ti6Al4V were investigated. Cutting simulation and experimental results from UPSM were compared to those from CM.

We found that UPSM produces curled chips with vibration-induced textures, showing obvious localized chip-breaking features at a vibration amplitude of 8 μm. TUPSM produces fine fragmented chips, demonstrating its capability to maintain shear cutting even at a cutting width of 3 μm in variable-thickness machining. Compared to CM, UPSM minimizes surface defects such as scratches and scale, despite inducing slightly higher surface roughness due to its associated texturing effects.

As explored in both simulations and experiments with USPM, the ultrasonic ironing and impact effects of the cutting edge produce a significant surface strengthening effect. At a vibration amplitude of 8 μm, the surface residual compressive stress and the thickness of the subsurface plastic deformation layer increase by 47.4% and 91.5%, respectively. Furthermore, the strengthening effect is enhanced even more following TUPSM.

UPSM significantly enhances the fatigue life of specimens, causing the initiation sites of fatigue sources to shift from the surface to the subsurface. At a vibration amplitude of 8 μm, UPSM and TUPSM increase the fatigue life by factors of 3.38 and 3.76, respectively.

Thus, UPSM and TUPSM have been demonstrated as promising titanium alloy strengthening methods, which effectively improve the fatigue performance of components with thin-walled structures while facilitating precision machining.

Acknowledgments

This work is supported by the National Natural Science Foundation of China (Nos. 91960203 and 52375399) and the Natural Science Foundation of Beijing Municipality (No. Z230004), China.

Author contributions

Lianxing LIU, Daxi GENG, and Deyuan ZHANG designed the research. Lianxing LIU, Enze YING, and Zhefei SUN processed the corresponding data. Lianxing LIU wrote the manuscript. Xinggang JIANG, Daxi GENG, and Deyuan ZHANG revised and edited the final version.

Conflict of interest

Lianxing LIU, Xinggang JIANG, Enze YING, Zhefei SUN, Daxi GENG, and Deyuan ZHANG declare that they have no conflict of interest.

References

Brehl DE, Dow TA, 2008. Review of vibration-assisted machining. *Precision Engineering*, 32(3):153-172.

https://doi.org/10.1016/j.precisioneng.2007.08.003

Celaya A, de Lacalle LNL, Campa FJ, et al., 2010. Ultrasonic assisted turning of mild steels. *International Journal of Materials and Product Technology*, 37(1-2):60-70. https://doi.org/10.1504/ijmpt.2010.029459

de la Maza García ÁS, de Lacalle Marcaide LNL, de Pissón Caruncho GM, 2025. Prestress assisted machining: achieving high surface integrity in thin wall milling. *Results in Engineering*, 26:105491. https://doi.org/10.1016/j.rineng.2025.105491

la Monaca A, Murray JW, Liao ZR, et al., 2021. Surface integrity in metal machining-part II: functional performance. *International Journal of Machine Tools and Manufacture*, 164:103718. https://doi.org/10.1016/j.ijmachtools.2021.103718

Li GX, Xie WB, Wang HT, et al., 2023. Optimizing processing parameters and surface quality of TC18 via ultrasonic-assisted milling (UAM): an experimental study. *Micromachines (Basel)*, 14(6):1111. https://doi.org/10.3390/mi14061111

Li X, Yang SL, Lu ZH, et al., 2020. Influence of ultrasonic peening cutting on surface integrity and fatigue behavior of Ti-6Al-4V specimens. *Journal of Materials Processing Technology*, 275:116386. https://doi.org/10.1016/j.jmatprotec.2019.116386

Liao ZR, la Monaca A, Murray J, et al., 2021. Surface integrity in metal machining-Part I: fundamentals of surface characteristics and formation mechanisms. *International Journal of Machine Tools and Manufacture*, 162:103687. https://doi.org/10.1016/j.ijmachtools.2020.103687

Liu JJ, Jiang XG, Han X, et al., 2019. Influence of parameter matching on performance of high-speed rotary ultrasonic elliptical vibration-assisted machining for side milling of titanium alloys. *The International Journal of Advanced Manufacturing Technology*, 101(5-8):1333-1348. https://doi.org/10.1007/s00170-018-3006-6

Liu LX, Jiang XG, Ying EZ, et al., 2025. High-performance milling of Ti-6Al-4V through rotary ultrasonic elliptical milling with anticlockwise elliptical vibration. *Journal of Zhejiang University-SCIENCE A*, 26(8):707-722. https://doi.org/10.1631/jzus.A2500007

Liu YH, Geng DX, Shao ZY, et al., 2021. A study on strengthening and machining integrated ultrasonic peening drilling of Ti-6Al-4V. *Materials & Design*, 212:110238. https://doi.org/10.1016/j.matdes.2021.110238

Liu YH, Zhang DY, Geng DX, et al., 2023. Ironing effect on surface integrity and fatigue behavior during ultrasonic peening drilling of Ti-6Al-4V. *Chinese Journal of Aeronautics*, 36(5):486-498. https://doi.org/10.1016/j.cja.2022.12.009

Lu HF, Wang Z, Cai J, et al., 2021. Effects of laser shock peening on the hot corrosion behaviour of the selective laser melted Ti6Al4V titanium alloy. *Corrosion Science*, 188:109558. https://doi.org/10.1016/j.corsci.2021.109558

Lu HF, Wu LJ, Wei HL, et al., 2022. Microstructural evolution and tensile property enhancement of remanufactured Ti6Al4V using hybrid manufacturing of laser directed energy deposition with laser shock peening. *Additive Manufacturing*, 55:102877. https://doi.org/10.1016/j.addma.2022.102877

Lü QQ, Chai YB, Yang LQ, et al., 2023. Experimental study on cutting force and surface integrity of TC4 titanium alloy with longitudinal ultrasonic-assisted milling. *Coatings*, 13(10):1725. https://doi.org/10.3390/coatings13101725

Medvedev AE, Lui EW, Edwards D, et al., 2021. Improved ballistic performance of additively manufactured Ti6Al4V with α-β lamellar microstructures. *Materials Science and Engineering: A*, 825:141888. https://doi.org/10.1016/j.msea.2021.141888

Moriwaki T, Shamoto E, 1995. Ultrasonic elliptical vibration cutting. *CIRP Annals*, 44(1):31-34. https://doi.org/10.1016/S0007-8506(07)62269-0

Ni CB, Zhu LD, 2020. Investigation on machining characteristics of TC4 alloy by simultaneous application of ultrasonic vibration assisted milling (UVAM) and economical-environmental MQL technology. *Journal of Materials Processing Technology*, 278:116518. https://doi.org/10.1016/j.jmatprotec.2019.116518

Novovic D, Dewes RC, Aspinwall DK, et al., 2004. The effect of machined topography and integrity on fatigue life. *International Journal of Machine Tools and Manufacture*, 44(2-3):125-134. https://doi.org/10.1016/j.ijmachtools.2003.10.018

Pang Y, Feng PF, Wang JJ, et al., 2021. Performance analysis of the longitudinal-torsional ultrasonic milling of Ti-6Al-4V. *The International Journal of Advanced Manufacturing Technology*, 113(5-6):1255-1266. https://doi.org/10.1007/s00170-021-06682-7

Qin Z, Li B, Chen R, et al., 2023. Effect of shot peening on high cycle and very high cycle fatigue properties of Ni-based superalloys. *International Journal of Fatigue*, 168:107429. https://doi.org/10.1016/j.ijfatigue.2022.107429

Rodríguez A, de Lacalle LNL, Celaya A, et al., 2012. Surface improvement of shafts by the deep ball-burnishing technique. *Surface and Coatings Technology*, 206(11-12):2817-2824. https://doi.org/10.1016/j.surfcoat.2011.11.045

Rodríguez A, Calleja A, de Lacalle LNL, et al., 2019. Burnishing of FSW aluminum Al-Cu-Li components. *Metals*, 9(2):260. https://doi.org/10.3390/met9020260

Rodríguez A, de Lacalle LNL, Pereira O, et al., 2020. Isotropic finishing of austempered iron casting cylindrical parts by roller burnishing. *The International Journal of Advanced Manufacturing Technology*, 110(3-4):753-761. https://doi.org/10.1007/s00170-020-05894-7

Seenath AA, Sarhan AAD, 2024. A state-of-the-art review on cutting tool materials and coatings in enhancing the tool performance in machining the superior nickel-based superalloys. *Arabian Journal for Science and Engineering*, 49(8):10203-10236. https://doi.org/10.1007/s13369-024-08745-9

Shamoto E, Moriwaki T, 1999. Ultraprecision diamond cutting

of hardened steel by applying elliptical vibration cutting. *CIRP Annals*, 48(1):441-444. https://doi.org/10.1016/S0007-8506(07)63222-3

Suárez A, Veiga F, de Lacalle LNL, et al., 2016. Effects of ultrasonics-assisted face milling on surface integrity and fatigue life of Ni-alloy 718. *Journal of Materials Engineering and Performance*, 25(11):5076-5086. https://doi.org/10.1007/s11665-016-2343-6

Suárez A, Veiga F, Polvorosa R, et al., 2019. Surface integrity and fatigue of non-conventional machined alloy 718. *Journal of Manufacturing Processes*, 48:44-50. https://doi.org/10.1016/j.jmapro.2019.09.041

Sun ZF, Geng DX, Guo HL, et al., 2024. Introducing transversal vibration in twist drilling: material removal mechanisms and surface integrity. *Journal of Materials Processing Technology*, 325:118296. https://doi.org/10.1016/j.jmatprotec.2024.118296

Teimouri R, 2025. A framework toward fatigue life modeling of machining process verified in burnishing. *Mechanical Systems and Signal Processing*, 223:111923. https://doi.org/10.1016/j.ymssp.2024.111923

Teimouri R, Grabowski M, 2024. Mechanistic model of fatigue in ultrasonic assisted machining. *Materials (Basel)*, 17(19): 4889. https://doi.org/10.3390/ma17194889

Teimouri R, Grabowski M, 2025. Effect of ultrasonic vibration on fatigue life of inconel 718 machined by high-speed milling: physics-enhanced machine learning approach. *Mechanical Systems and Signal Processing*, 224:112115. https://doi.org/10.1016/j.ymssp.2024.112115

Teimouri R, Skoczypiec S, 2024. A bottom-up multi-physics model correlating burnishing factors to fatigue life. *Measurement*, 234:114872. https://doi.org/10.1016/j.measurement.2024.114872

Teimouri R, Amini S, Guagliano M, 2019. Analytical modeling of ultrasonic surface burnishing process: evaluation of residual stress field distribution and strip deflection. *Materials Science and Engineering: A*, 747:208-224. https://doi.org/10.1016/j.msea.2019.01.007

Wang GY, Xu WY, Li CH, et al., 2024. Study on design of conical arc side-edge milling cutter and cutting performance under ultrasonic-assisted condition. *The International Journal of Advanced Manufacturing Technology*, 132(3-4):1411-1423. https://doi.org/10.1007/s00170-024-13423-z

Wang Y, Huang S, Sheng J, et al., 2024. Strengthening effect of laser peening on fatigue performance and life extension of laser cladded IN718 nickel-based alloy parts. *International Journal of Fatigue*, 180:108081. https://doi.org/10.1016/j.ijfatigue.2023.108081

Wang YJ, Hao EK, Zhao XQ, et al., 2022. Effect of microstructure evolution of Ti6Al4V alloy on its cavitation erosion and corrosion resistance in artificial seawater. *Journal of Materials Science & Technology*, 100:169-181. https://doi.org/10.1016/j.jmst.2021.06.005

Wang ZM, Jia YF, Zhang XC, et al., 2019. Effects of different mechanical surface enhancement techniques on surface integrity and fatigue properties of Ti-6Al-4V: a review. *Critical Reviews in Solid State and Materials Sciences*, 44(6): 445-469. https://doi.org/10.1080/10408436.2018.1492368

Xue NP, Wu Q, Zhang Y, et al., 2023. Review on research progress and comparison of different residual stress strengthening methods for titanium alloys. *Engineering Failure Analysis*, 144:106937. https://doi.org/10.1016/j.engfailanal.2022.106937

Yang ZC, Zhu LD, Zhang GX, et al., 2020. Review of ultrasonic vibration-assisted machining in advanced materials. *International Journal of Machine Tools and Manufacture*, 156:103594. https://doi.org/10.1016/j.ijmachtools.2020.103594

Yao J, Li X, Du BR, et al., 2024. Research status of influence mechanism of surface integrity on fatigue behavior of metal workpieces: a review. *The International Journal of Advanced Manufacturing Technology*, 131(7-8):3401-3419. https://doi.org/10.1007/s00170-024-13195-6

Ying EZ, Zhou ZH, Geng DX, et al., 2024. High-efficiency ultrasonic assisted drilling of CFRP/Ti stacks under non-separation type and dry conditions. *Journal of Zhejiang University-SCIENCE A*, 25(4):275-291. https://doi.org/10.1631/jzus.A2300227

Yuan X, Yue ZF, Wen SF, et al., 2015. Numerical and experimental investigation of the cold expansion process with split sleeve in titanium alloy TC4. *International Journal of Fatigue*, 77:78-85. https://doi.org/10.1016/j.ijfatigue.2015.03.014

Zhang GH, Lu XF, Li JQ, et al., 2022. In-situ grain structure control in directed energy deposition of Ti6Al4V. *Additive Manufacturing*, 55:102865. https://doi.org/10.1016/j.addma.2022.102865

Zhang ZM, Tong JL, Zhao JS, et al., 2021. Experimental study on surface residual stress of titanium alloy curved thin-walled parts by ultrasonic longitudinal-torsional composite milling. *The International Journal of Advanced Manufacturing Technology*, 115(4):1021-1035. https://doi.org/10.1007/s00170-021-07234-9

Zheng K, Liao WH, Dong Q, et al., 2018. Friction and wear on titanium alloy surface machined by ultrasonic vibration-assisted milling. *Journal of the Brazilian Society of Mechanical Sciences and Engineering*, 40(9):411. https://doi.org/10.1007/s40430-018-1336-9

Electronic supplementary materials

Sections S1–S3, Table S1, Figs. S1–S3